**RESEARCH PAPER**

# Experimental and Numerical Studies on Seismic Behavior of Composite Frames with Initial Heavy Load Conditions

Li Zhou[1,2] · Yi-sheng Su[1]

## Abstract
This study investigates the seismic behavior of composite frames with initial heavy load conditions. Two frame specimens consisting of square concrete-filled steel tube (CFST) columns and steel-reinforced concrete (SRC) deep beams were fabricated and poured using ordinary concrete and high-strength concrete, respectively. Thereafter, the two specimens were tested under cyclic loadings, and the failure models, hysteretic behavior, bearing capacity, ductility, and accumulated energy dissipation of the specimens were investigated in detail. The experimental results revealed that both of the specimens failed owing to the local buckling at the column ends. This kind of composite frame has good seismic performance and can be regarded as a high-ductility structure. Moreover, a finite element (FE) model was developed and verified by the experimental results. The effects of the typical parameters, such as the material strength and axial compression ratio, were studied using the FE model. The parametric study demonstrates that increasing the yield strength of the steel tube can effectively improve the ultimate bearing capacity of the composite frame and that decreasing the axial compression ratio is a valid method for improving the ductility of the structure.

**Keywords** Composite frame · Seismic behavior · Heavy load · Experimental study · Numerical study

## 1 Introduction

The damage or collapse of structures caused by earthquakes can result in fatalities and large economic loss. The recent massive earthquakes in China, Japan, and other countries have caused serious damage to structures. Among these damaged structures, structures subjected to heavy loads suffered great damage, such as the column-cap beam frame in bridges and the transfer structure in tall buildings (Zhao et al. 2009; Bhattacharya et al. 2018). The significant characteristic of this kind of frame is that the beam must support the superstructures, similar to the foundations of a structure, which means that the beam experiences large vertical loads. Moreover, concentrated stresses and large lateral displacements may occur on the structure, owing to the actions of the horizontal loads. Hence, a more stringent design is needed to

ensure the demands of the bearing capacity and the ductility (Li et al. 2003). Figure 1 shows the applications of this kind of structure in practical engineering.

In a bridge system, the damage of the column-cap beam frame can compromise the structural safety of the whole bridge system. To improve the seismic performance of the frame, several techniques are applied. Ichikawa et al. (2016), Mohebbi et al. (2015), and Wang et al. (2016) have focused on the beneficial effect of ultra-high-performance concrete (UHPC) on the seismic behavior of piers. They all concluded that UHPC used in the piers or the plastic hinge regions of the column can reduce the seismic damage. Furthermore, the bearing capacity and the ductility can be significantly improved. Bazaez and Dusicka (2016), El-Bahey and Bruneau (2011), and Dong et al. (2017) added buckling-restrained braces (BRBs) to column-cap beam frames to improve the energy dissipation of the frames. It was demonstrated that utilizing BRBs in column-cap beam frames can increase the displacement ductility of the structure. Moreover, the seismic damage to the frame can be controlled in an acceptable range. Stephens et al. (2018), Fujikura and Bruneau (2012), Montejo et al. (2012) and Fulmer et al. (2016) investigated a bridge substructure consisting of

✉ Yi-sheng Su
suyisheng@gxu.edu.cn

1 College of Civil Engineering and Architecture, Guangxi University, Nanning 530004, China

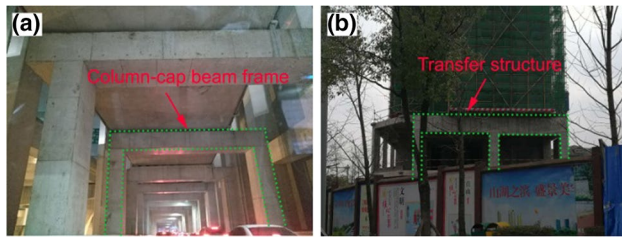2 College of Architecture and Urban Planning, Guizhou University, Guiyang 550003, China

**Fig. 1** Practical engineering

CFST piers; the behaviors of the CFST frames, members, and connections were analyzed in detail. Compared with the traditional reinforced concrete bridges, the CFST column-cap beam frame exhibited the advantages of convenient construction and good ductility.

Regarding the transfer structures in buildings, Li et al. (2003) conducted a seismic assessment for a low-rise building with a transfer structure in Hong Kong. The results indicated that the ductility of the transfer structures, at both the member and global levels, was relatively low. This may lead to a sudden brittle-type failure of the transfer structure. Shahnewaz et al. (2012) performed a pushover analysis and a time history analysis to investigate the seismic behavior of a transfer structure. The study showed a significant strength deficit in the transfer beam under the actions of different earthquake waves. Additionally, the studies conducted by Su et al. (2002) showed that the structural seismic assessments for transfer structures in low-to-moderate seismicity regions require the acute lack of ductility in mega-columns to be specifically considered. To enhance the bearing capacity and ductility of transfer structures, steel–concrete composite members were used for such frames recently. The behaviors of steel truss-reinforced concrete transfer beams were discussed in detail by Wu et al. (2011). The transfer structures comprising SRC members were investigated by Wang et al. (2011). In addition, the seismic behaviors of composite transfer frames were studied by Nie et al. (2017).

According to the aforementioned studies, the column-cap beam frame or transfer structure must have a high bearing capacity and ductility. Although studies have proven that the UHPC materials and BRBs can effectively improve the bearing capacity and ductility of the structure, their applications are limited owing to high construction costs and restricted internal spaces. Although the steel–concrete composite structure has been confirmed to have a high bearing capacity and ductility (Roeder et al. 2018; Zhou and Su 2018), the studies and applications of composite frames in bridge substructures are limited, especially in the transfer structures of buildings. Therefore, in consideration of the construction convenience of square section members in practical engineering, the present study focuses on composite frames with square CFST columns and SRC beams. Two

composite frame specimens with different concrete strengths are tested; the failure modes, hysteretic behaviors, energy dissipations, and ductility of all the specimens are evaluated. Furthermore, an efficient FE analysis model is established to simulate the behavior of this kind of frame.

## 2 Experimental Program

### 2.1 Test Specimens

Two specimens with a scale of 1:4 to the actual structure were tested (denoted as F-1 and F-2). The dimensions, steel tubes, I-shaped steel, and reinforcements of the two specimens were the same. The only difference between the two specimens was the concrete strength. Figure 2 shows the dimensions and details of the specimens.

Regarding the connections between the beam and column, the through-beam connection type was adopted according to the Chinese code GB50936 (2014). In consideration of the mechanical behavior of SRC deep beams, the demands for shear strength are significantly higher than those for bending strength. Therefore, only the shaped steel web and longitudinal steel bars passed through the steel tubes. The frame specimens were fabricated in a professional processing factory. First, small openings corresponding to the sections of the steel web and steel bars were cut at the steel tube wall. Then, the I-shaped steel and longitudinal steel bars were installed onto the steel tube by crossing the openings. Finally, the contact positions were welded with a 6-mm weld line; the welding modes on both sides of the steel tube were the same. Figure 3 shows the details of the connection.

### 2.2 Material Properties

Improving the concrete strength in CFST structures increases the bearing capacity (Sakino et al. 2004). In China, the most commonly used concrete in CFST structures ranges from C30 to C60 (Han 2007), which is compatible with the commonly used steel, improving the structural performance (Han et al. 2014). In the present experiment, C40 and C60 fine aggregate concretes were used for specimens F-1 and F-2, respectively. C60 concrete is defined as a high-strength concrete according to the Chinese code JGJ/T-281 (2012) and is commonly used in practical engineering. Property tests were performed on the concrete according to GB/T50081 (2016), and the average cubic compressive strength $f_{cu}$ (cube size 150 mm × 150 mm × 150 mm), axial compressive strength $f_{ck}$ (prism size 150 mm × 150 mm × 300 mm), and Young's modulus $E_c$ are presented in Table 1.

Q235 steel was used for the I-shaped steel and steel tube, and only the steel tube was hardened. HPB300 and HRB400 steel was used for the stirrup and longitudinal steel bars,
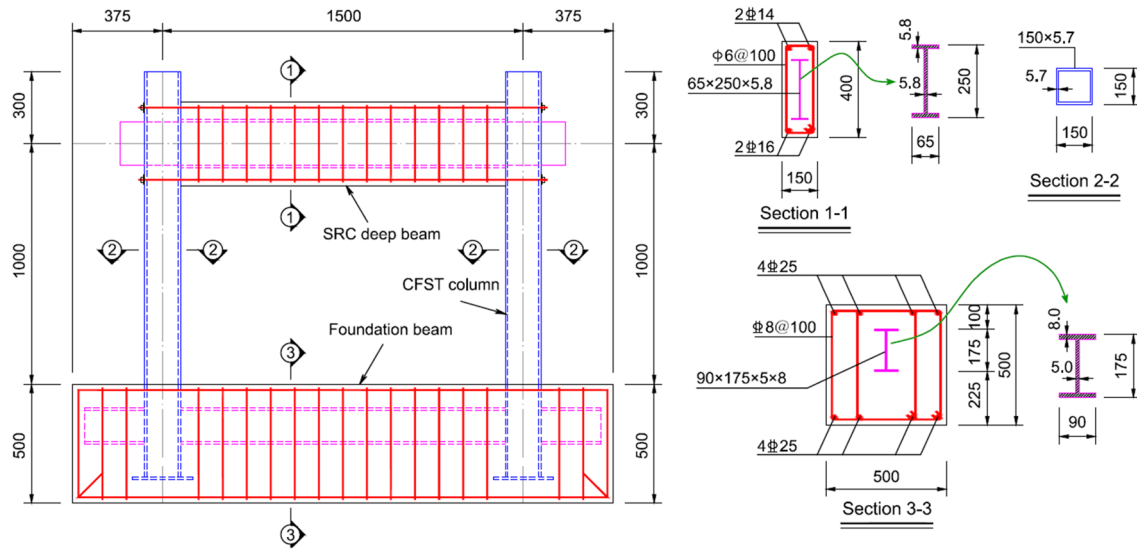
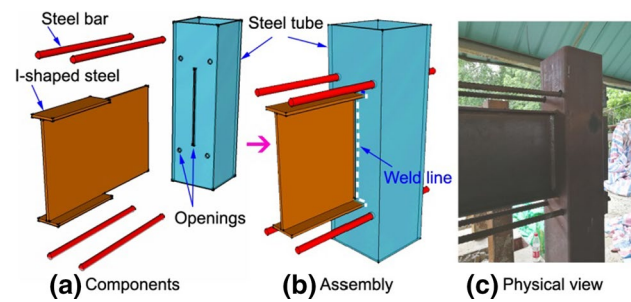**Fig. 2** Dimensions and details of specimens (unit: mm)



**Fig. 3** Details of the connection

**Table 1** Mechanical properties of the concrete

| Concrete type | $f_{cu}$ (N/mm²) | $f_{ck}$ (N/mm²) | $E_c$ (N/mm²) |
|---|---|---|---|
| C40 | 41.7 | 32.7 | $3.01 \times 10^4$ |
| C60 | 59.8 | 40.6 | $3.76 \times 10^4$ |

respectively. Tensile coupon tests were performed according to GB/T228 (2002), and the values of the yield strength

$f_y$, ultimate tensile strength $f_u$, and elastic modulus $E_s$ are presented in Table 2.

### 2.3 Determination of Vertical Loads

Three vertical loads must be imposed on the frame: One is applied to the mid-span of the SRC deep beam, and the remaining two are imposed on the column. To determine the values of the vertical loads applied to the beam, two beam specimens denoted as B-1 and B-2 were fabricated and cured along with the frame specimens. The dimensions and materials of B-1 and B-2 were the same as those of the corresponding SRC deep beams in frames F-1 and F-2, respectively. Vertical loading tests were conducted for the beam specimens by using an electro-hydraulic servo loading system. Figure 4 shows the force–deflection curves of the two beam specimens, and Fig. 5 illustrates the failure modes. As shown in Fig. 4, the yield bearing capacities of B-1 and B-2 were 499.7 and 535.4 kN, respectively. Considering the influence of load factors in practical engineering design (GB 50009 2012), an 80% yield bearing capacity was selected as the actual loading value applied to the mid-span of the beam; accordingly,

**Table 2** Mechanical properties of the steel

| Steel type | Thickness, [diameter] (mm) | $f_y$ (N/mm²) | $f_u$ (N/mm²) | $E_s$ (N/mm²) |
|---|---|---|---|---|
| I-shaped steel | 5.8 | 295.5 | 422.9 | $1.98 \times 10^5$ |
| Steel tube | 5.7 | 320.5 | 479.0 | $2.14 \times 10^5$ |
| Stirrup | [6.0] | 369.7 | 529.9 | $2.11 \times 10^5$ |
| Longitudinal steel bar | [14.0] | 410.0 | 614.3 | $2.05 \times 10^5$ |
| | [16.0] | 395.2 | 596.1 | $2.10 \times 10^5$ |

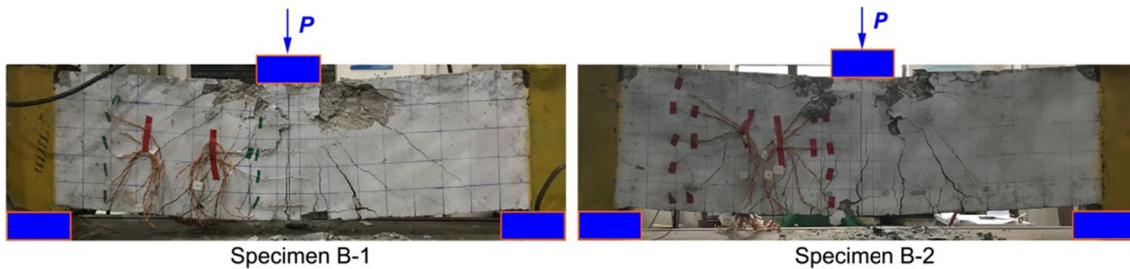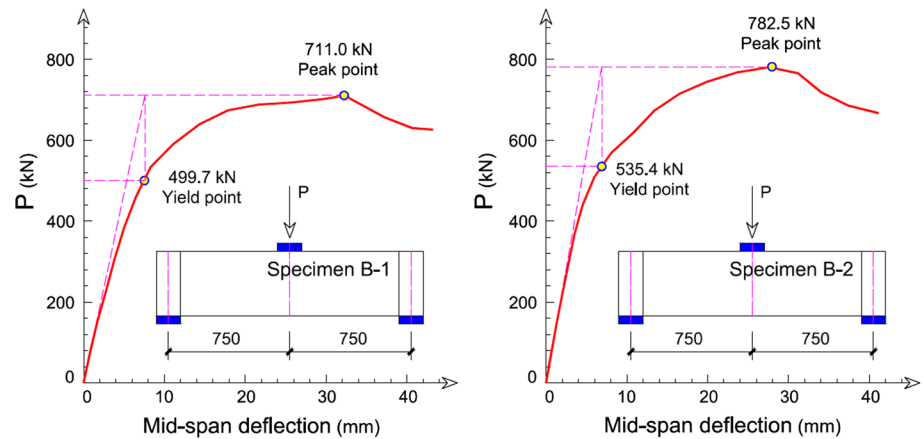**Fig. 4** Force–deflection curves of B-1 and B-2



**Fig. 5** Failure modes of B-1 and B-2

the vertical loads applied to the beams in frame specimens F-1 and F-2 were 400 and 430 kN, respectively.

The axial forces imposed on columns are determined using the calculation formula of the axial compression ratio:

$$n = N/(f_y A_s + f_{ck} A_c) \tag{1}$$

where $N$ is the axial force, $f_y$ is the yielding strength of the steel tube, $f_{ck}$ is the axial compressive strength of the concrete, and $A_c$ and $A_s$ are the cross-sectional areas of the core concrete and steel tube, respectively.

The axial compression ratio $n = 0.4$ was selected for both of the frame specimens, according to the suggested value in reference (Su et al. 2002). The calculated $N$ values for the columns of specimens F-1 and F-2 were 680 and 735 kN, respectively. After the loads transferred from the beams were subtracted, the actual vertical loads imposed on the columns in frame specimens F-1 and F-2 were 480 and 520 kN, respectively.

### 2.4 Experimental Setup

Each frame specimen was subjected to a constant axial load to simulate the axial loads transferred from the superstructure, as well as a cyclic horizontal load to simulate the earthquake actions. Figures 6 and 7 present physical and schematic views, respectively, of the experimental setup. The



**Fig. 6** Physical view of the experimental setup

specimens were tested in the Key Laboratory of the China Ministry of Education. First, the specimen was installed on the reaction platform; the foundation beam was fastened to the strong floor through the reaction beams and high-strength steel rods. Two fixing devices were mounted on the lateral sides of the columns through the steel rods. Then, the vertical loads were imposed on the specimen through three hydraulic jacks; gliding devices were installed on the hydraulic jacks to reduce the friction between the jacks and the rigid reaction frame. Finally, a cyclic load in the horizontal direction was imposed at the end of the fixing device
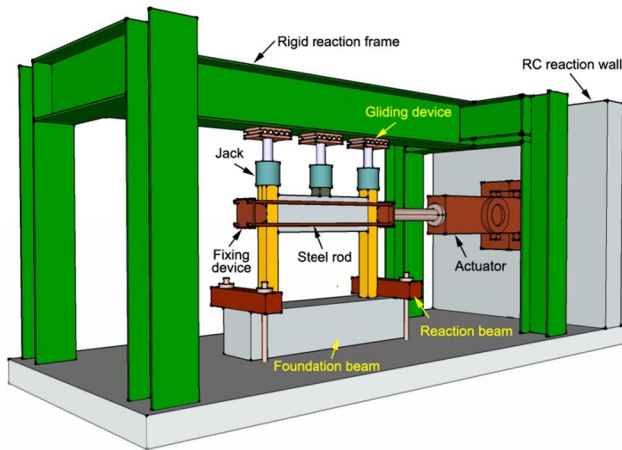
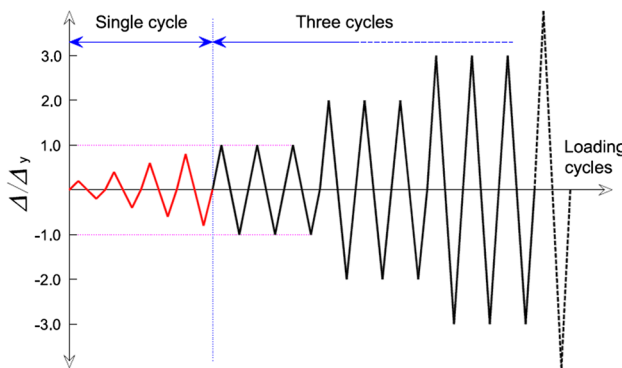**Fig. 7** Schematic view of the experimental setup



**Fig. 8** Lateral loading history of the specimens

through a servo-controlled hydraulic actuator with a maximum load capacity of 1000 kN.

## 2.5 Loading History

Regarding the lateral loading schedule, the displacement loading protocol was applied during the cyclic loading process in accordance with the ATC-24 (1992) guidelines, as shown in Fig. 8. First, the yield displacement ($\Delta_y$) was determined via FE analysis. Then, a single cycle was applied to the specimen at each of the following displacement levels: $0.2\Delta_y$, $0.4\Delta_y$, $0.6\Delta_y$, and $0.8\Delta_y$. After the specimen entered its yield stage, three cycles were employed at integer multiples of $\Delta_y$.

## 3 Experimental Results and Discussion

### 3.1 Experimental Observations and Failure Modes

The two tested specimens exhibited similar experimental results, including the failure modes. Both of them failed in local buckling at the column ends, which is consistent with the design requirements of JTG/T B02-01(2008) (Clauses 6.2.1 and 6.2.2: the columns in bridge substructures are suitable to be designed as ductility members, and the potential plastic hinges shall be located at the ends of the columns.).

Figure 9 shows the experimental observations for the two specimens. As shown in Fig. 9a and b, the SRC deep beams in the two frames had essentially the same crack pattern. During the vertical loading stage, bending cracks were observed at the mid-span of the beams, and the inclination angle was larger at positions closer to the beam ends. When the specimens entered the lateral loading stage, some new diagonal cracks were observed in the shear spans, and the existing cracks kept propagating with the increase in the lateral load. When the lateral displacement increased to $\Delta_y$, the diagonal cracks progressed in an inclined manner toward
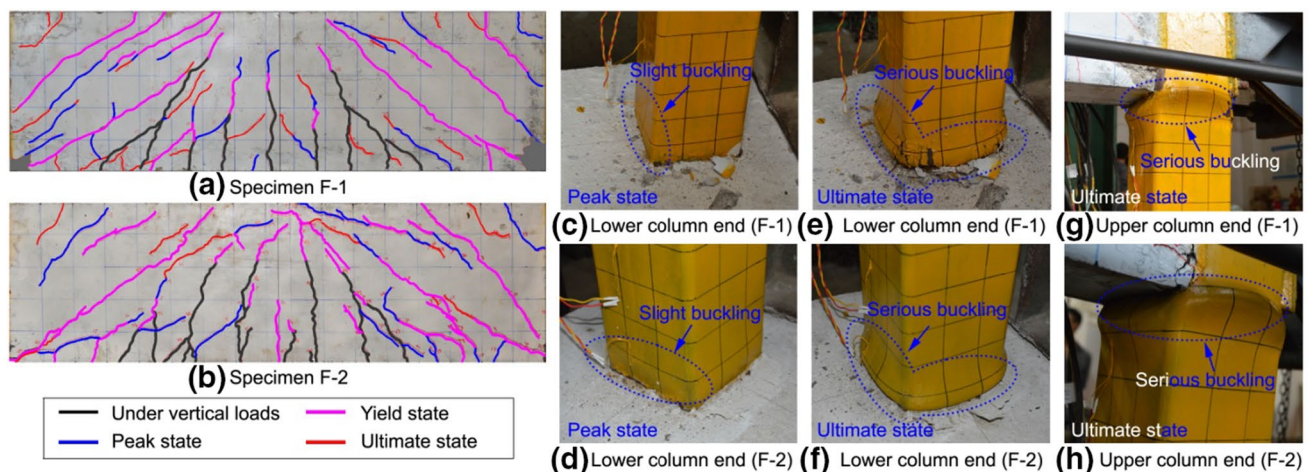


**Fig. 9** Failure patterns of the specimens

the loading point, as well as the beam supports. When the lateral displacement reached approximately 20 mm (the peak state), more diagonal cracks appeared with the increase in the lateral load. Additionally, concrete crushing occurred at the bottom of the two beam ends in specimen F-1, whereas no such phenomenon was observed in specimen F-2. When the lateral displacement reached approximately 30 mm (the ultimate state), the existing diagonal cracks propagated very slowly with the further increase in the lateral displacement, and a few new bending cracks were formed at the top of the beam ends.

For the CFST columns, no local buckling was observed before the peak state. When the specimens reached their peak state, slight local buckling was observed on the bottom of the CFST columns (see Fig. 9c and d). When the specimens reached their ultimate state, both the top and bottom of the CFST columns exhibited serious local buckling, as illustrated in Fig. 9e, f, g, and h.

## 3.2 Hysteresis Curve and Skeleton Curve

The measured lateral load versus lateral displacement hysteresis curves of the two specimens are shown in Fig. 10. The hysteresis curves of the two composite frame specimens are smooth and full, with shuttle-shaped hysteresis loops. In general, the hysteresis curve outlines of F-2 are larger than those of F-1, as the concrete strength of F-2 is higher than that of F-1.

The skeleton curves for the two specimens are shown in Fig. 11. Three typical characteristic points are extracted in accordance with Fig. 11a shown in the JGJ/T 101 (2015). In Fig. 11a, points 1, 2, and 3 represent the yield point, peak point, and ultimate point of the skeleton curve, respectively. Table 3 presents the major characteristic values from the skeleton curves of the tested specimens. As indicated in Fig. 11 and Table 3, the skeleton curves can be divided into an elastic stage, an elastic–plastic stage, and a failure stage. In the elastic stage, the yield displacements of F-1 in
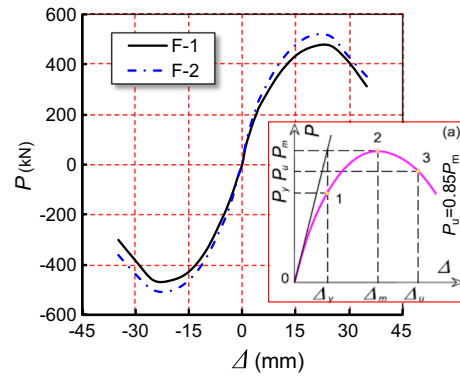


**Fig. 11** Skeleton curves

the positive direction (PD) and negative direction (ND) are 8.31 and 8.46 mm, respectively, which are 5.9% and 3.4% higher than those for F-2. This indicates that F-2 has a higher initial stiffness, as the elastic modulus of concrete for F-2 is higher than that for F-1. (The bending stiffness of the column for F-2, calculated as $E_sI_s + E_cI_c$, is approximately $3.62 \times 10^{12}$ N mm$^2$, which is 6.3% higher than that of F-1.) In the peak state, the peak bearing capacities of F-2 in the PD and ND are 517.88 and 503.26 kN, respectively, which are 8.4% and 7.6% higher than those of F-1, respectively. The reason for this is that F-2 has higher concrete strength. In the failure stage, the curve slopes for both specimens are relatively consistent, indicating that the contributions of concrete in the frames are diminished.

## 3.3 Ductility

The ductility of a structure reflects the capacity of plastic deformation. It is a significant index for the seismic design. In general, the ductility factor $\mu$ can be used to evaluate the ductility performance of a structure, which is defined as follows:

$$\mu = \Delta_u/\Delta_y \qquad (2)$$
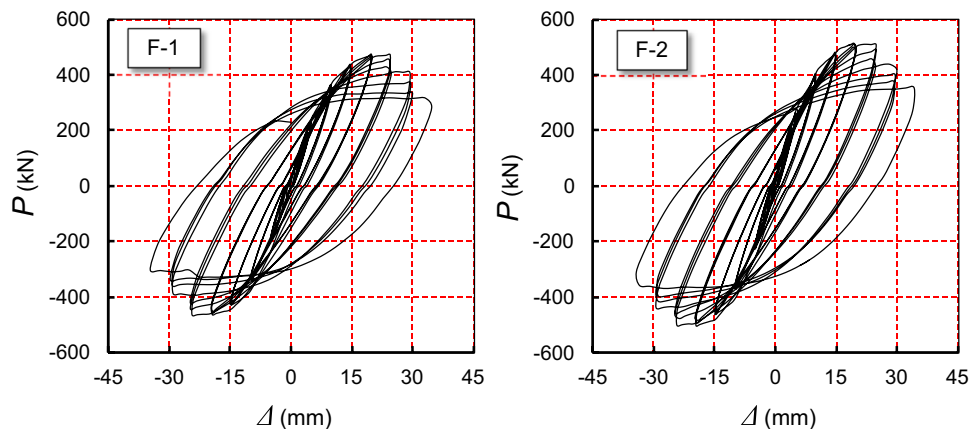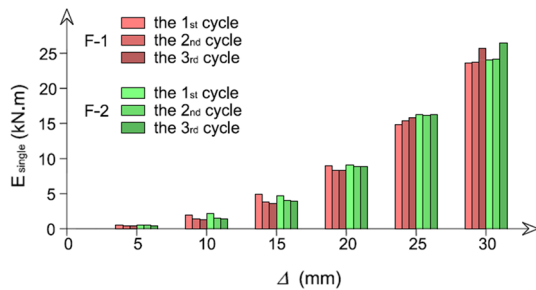
**Fig. 10** Hysteresis curves

**Table 3** Characteristic values on skeleton curves

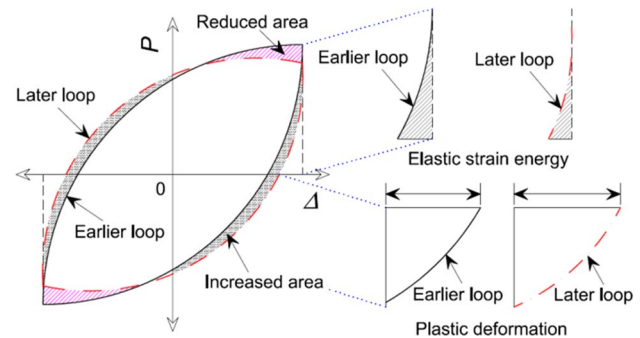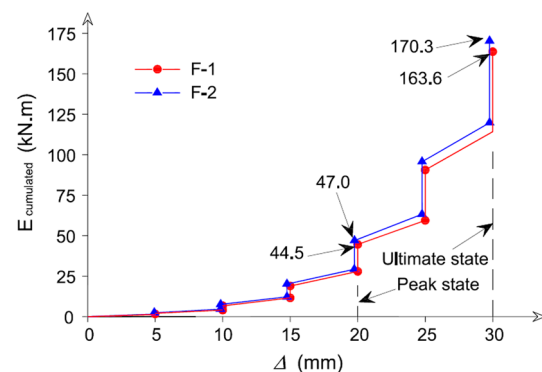| Specimen | Yield state | | Peak state | | Ultimate state | | Ductility |
|---|---|---|---|---|---|---|---|
| | $\Delta_y$ (mm) | $P_y$ (kN) | $\Delta_m$ (mm) | $P_m$ (kN) | $\Delta_u$ (mm) | $P_u$ (kN) | $\Delta_u/\Delta_y$ |
| F-1(+) | 8.31 | 319.92 | 21.47 | 474.30 | 30.27 | 403.16 | 3.64 |
| F-1(−) | −8.46 | −302.71 | −21.56 | −465.16 | −29.43 | −395.39 | 3.49 |
| F-2(+) | 7.82 | 347.33 | 21.39 | 517.88 | 29.37 | 440.20 | 3.75 |
| F-2(−) | −8.17 | −323.52 | −22.07 | −503.26 | −30.45 | −427.77 | 3.73 |

"(+)" and "(−)" represent "positive direction" and "negative direction," respectively



**Fig. 12** Dissipated energy of each cycle



**Fig. 13** Energy analysis of the hysteresis loops

where $\Delta_y$ is the yield displacement and $\Delta_u$ is the ultimate displacement. Table 3 presents the ductility factors of the two specimens. The ductility factors of F-2 are slightly higher than those of F-1 because of the smaller yield displacements of F-2, and the ductility factors of all the tested specimens are within the range of 3.49–3.75. Regarding the demands of the structural ductility, the structure with $\mu \geq 3$ was defined as a high-ductility structure according to the New Zealand design code NZS 1170.5 (2004). Hence, the specimens examined in this study can be considered as high-ductility structures.

## 3.4 Energy Dissipation

The energy dissipation capacity is an important index for assessing the seismic performance of a structure. To quantify the energy dissipation of the tested specimens, the dissipated energy of each cycle, which is equal to the area of the hysteresis loop, was calculated, as illustrated in Fig. 12. Analysis of the dissipated energy for each cycle in Fig. 12 reveals the following: (1) The dissipated energy of specimen F-2 at each loading cycle is slightly higher than that of specimen F-1. This is explained by the fact that increasing the concrete strength can enlarge the areas of the hysteresis loops, which corresponds to the improvement in the bearing capacity. (2) Before the specimen reaches its peak state, the dissipated energy for the first cycle is the highest among the three cycles, at each loading level. However, the reverse phenomenon was observed at the failure stage of the specimen, possibly owing to the



**Fig. 14** Accumulated dissipated energy of the specimens

reduction in the structural elastic strain energy as well as the increase in the structural plastic deformation, as illustrated in Fig. 13.

The accumulated dissipated energy of the two frame specimens throughout the loading process is shown in Fig. 14. It can be seen that the accumulated dissipated energy for F-2 is always slightly higher than that of F-1 during the whole loading process, and the accumulated dissipated energy for F-2 at the peak and ultimate states is approximately 5.3% and 3.9% higher than those of F-1, respectively; this is reasonable since the specimen with higher concrete strength can improve the bearing capacity, which leads to a larger hysteresis loops' area (see Fig. 12).
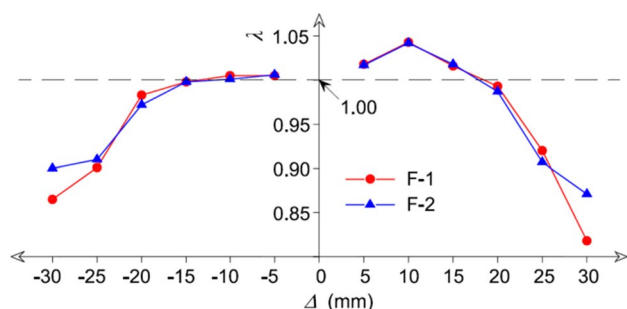
**Fig. 15** Evolution of the strength degradation

## 3.5 Strength Deterioration

To evaluate the strength deterioration of the specimens during the loading process, the deterioration coefficient $\lambda$ was adopted in accordance with Chinese code JGJ/T 101 (2015), which is defined as follows:

$$\lambda_i = P_i^3 / P_i^1 \tag{3}$$

where $P_i^1$ and $P_i^3$ are the maximum lateral loads recorded in the first and third hysteresis loops at the $i$th loading level, respectively. Figure 15 shows the deterioration coefficient $\lambda$ of the two specimens during the loading process.

As shown in Fig. 15, before the peak state, the deterioration coefficients of the two tested specimens are generally greater than 1.0 (ranging from 0.98 to 1.04), especially for the coefficients in the PD. A possible reason for this is that the lateral loading of the specimens leads to a hardening effect in the steel; this is consistent with the findings of Tao et al. (2013). Moreover, the deterioration coefficients of F-2 in the ultimate state are significantly smaller than those of F-1, indicating that F-2 has a higher residual bearing capacity.

## 3.6 Stiffness Degradation

The stiffness degeneration of a structure with respect to the increment in the lateral displacement is an important index for assessing the structural seismic performance, which can be evaluated through the stiffness degeneration coefficient $K$. The calculation formula is as follows:

$$K_i = \left( \left| P_i^+ \right| + \left| P_i^- \right| \right) \Big/ \left( \left| \Delta_i^+ \right| + \left| \Delta_i^- \right| \right) \tag{4}$$

where $P_i^+$ and $P_i^-$ are the positive and negative maximum lateral loads of the first loading cycle at the $i$th loading level, respectively, and $\Delta_i^+$ and $\Delta_i^-$ are the positive and negative maximum lateral displacements of the first loading cycle at the $i$th loading level, respectively.

Figure 16 shows the stiffness deterioration process for the two specimens. The following observations are made: (1) The structural stiffness of F-2 is higher than that of F-1 during the whole loading process, owing to the adoption of higher strength concrete; (2) the structural stiffness difference between F-1 and F-2 gradually decreased with the increase in the loading. When the specimens transition from the initial state to the yield, peak, and ultimate states, the stiffness difference values are found to decrease by 34.3, 67.2, and 82.8%, respectively. This indicates that the contributions of the concrete in the later loading stage are diminished, which is consistent with the findings of Zhou and Su (2018).

# 4 FE Modeling

## 4.1 General

To further investigate the seismic behavior of this kind of frame, the FE program ABAQUS was employed to conduct FE analysis. Figure 17 shows the FE meshes of the composite frame, and Fig. 18 shows the steel skeletons of the FE model.

In the FE model, eight-node reduced integral format three-dimensional solid elements with reduced integration (C3D8R) were used to simulate the steel tube, concrete, and loading plates; four-node shell elements (S4R) were used to simulate the I-shaped steels; and two-node truss elements (T3D2) were employed to simulate the steel bars. The bottom of the foundation beam was defined as a fixed end; the displacements in the $x$, $y$, and $z$ directions and the rotations around the $x$, $y$, and $z$-axes were all constrained. Five rigid loading plates and corresponding reference points were created for loading, and two loading steps were employed for the model. In the first step, the vertical loads were applied on the top of the columns and the mid-span of the beam. In the second step, lateral cyclic
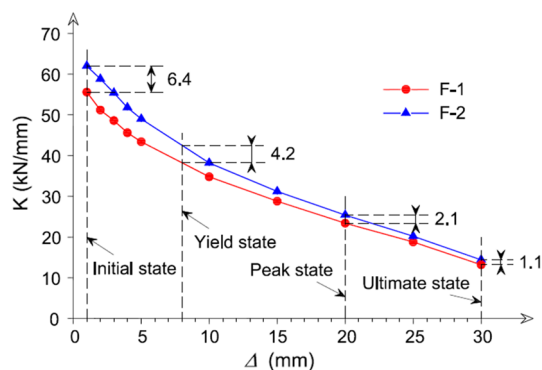


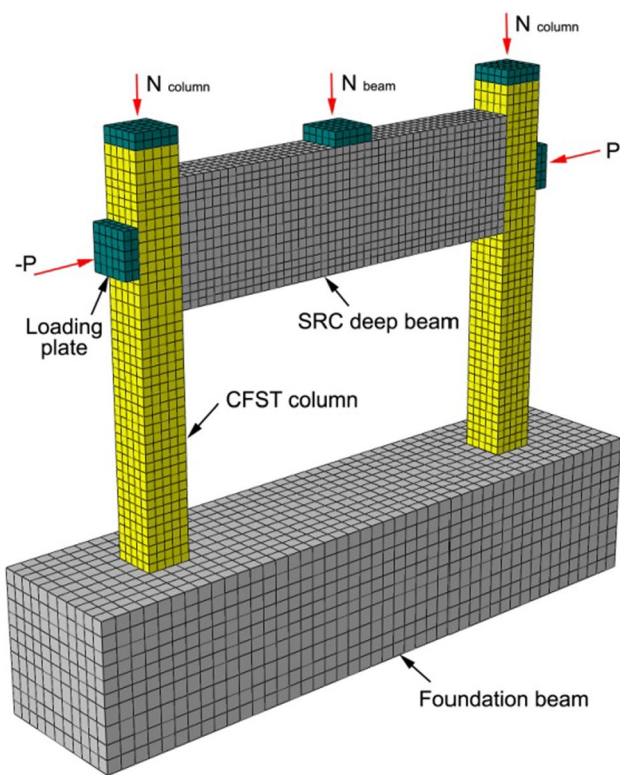**Fig. 16** Evolution of the stiffness degradation
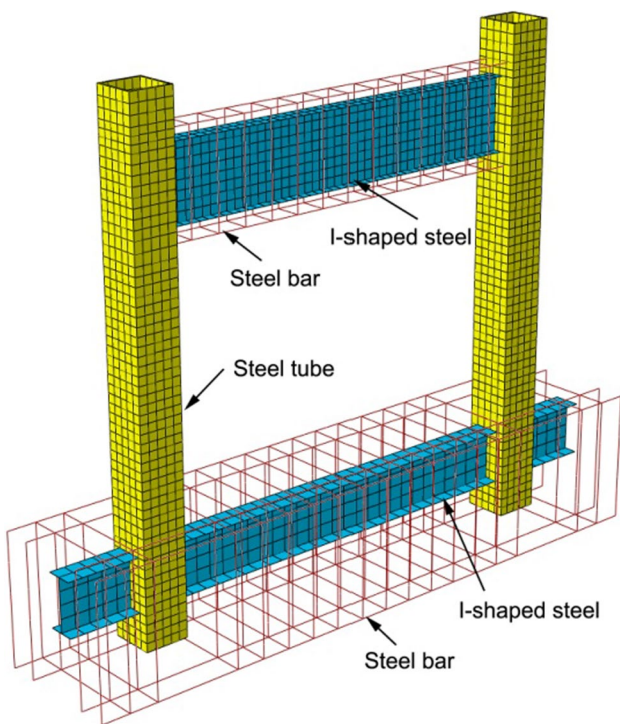
**Fig. 17** FE meshes of the composite frame



**Fig. 18** Steel skeletons of the FE model

loads were applied in the horizontal axis direction of the beam. Regarding the contact behaviors between different materials, a surface-to-surface contact interaction was employed at the interfaces of the steel tube and core concrete, the normal behavior was defined as "hard contact," and the tangential friction coefficient was taken as 0.45 (Chen et al. 2014). The "embedded region" function was adopted for embedding the steel bars and I-shaped steel beams in the whole model. The mesh size of the FE model affects the analysis accuracy and computational efficiency. According to the results of several pre-calculations, mesh sizes of 30 mm for the superstructure and 50 mm for the foundation beam were selected in this simulation.

## 4.2 Models for Material Properties

### 4.2.1 Material Modeling of Steel

The bilinear kinematic hardening model with a von Mises yield criterion and an associated plastic flow rule of steel was used to simulate the behavior of the steel. This model considers the Bauschinger effect, i.e., when the material enters its plastic development stage, the reverse loading leads to a decrease in the yield stress. For the elastic modulus of the steel materials, the measured values were employed (see Table 2), and the hardening modulus of all the materials was assumed to be $0.01E_s$, as shown in Fig. 19.
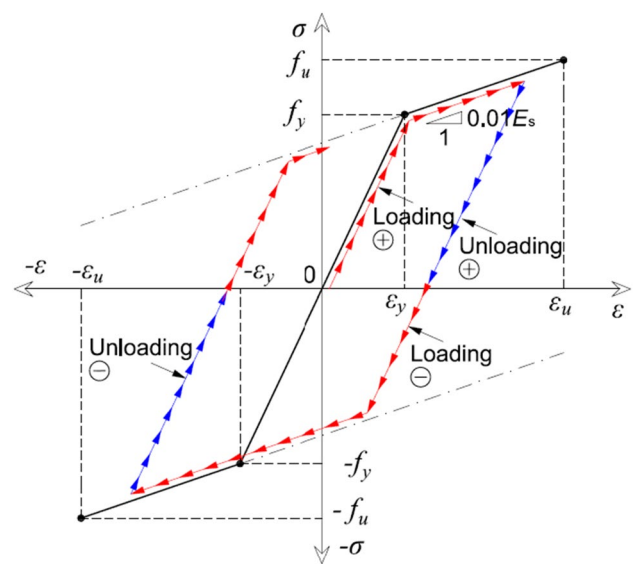


**Fig. 19** Stress–strain relationship for the steel

### 4.2.2 Material Modeling of Concrete

The concrete damaged plasticity model and the Willam–Warnke five-parameter failure criteria in ABAQUS were employed to simulate the concrete material. This model is suitable for simulating the inelastic behavior of materials under cyclic loading. For the dilation angle and other parameters, the values suggested by Li et al. (2018) were used. In this simulation, the constitutive models of unconfined concrete and confined concrete were applied for the beam concrete and column concrete, respectively. For the unconfined concrete, the constitutive model recommended by GB 50010 (2010) was adopted, which is expressed as follows.

- Constitutive model (compression):

$$\sigma = \begin{cases} \frac{\rho_c n}{n-1+x^n} E_c \varepsilon & (x \le 1) \\ \frac{\rho_c}{\alpha_c(x-1)^2+x} E_c \varepsilon & (x > 1) \end{cases} \tag{5}$$

where $\rho_c = f_c / E_c \varepsilon_{co}$, $n = E_c \varepsilon_{co}/(E_c \varepsilon_{co} - f_c)$, and $x = \varepsilon / \varepsilon_{co}$.

In the above equations, $f_c$ is the axial compressive strength of the concrete, $\varepsilon_{co}$ is the strain corresponding to $f_c$, $E_c$ is the Young's modulus of the concrete, and $\alpha_c$ is the parameter of the descending stage.

- Constitutive model (tension):

$$\sigma = \begin{cases} \rho_t(1.2 - 0.2x^5)E_c\varepsilon & (x \le 1) \\ \frac{\rho_t}{\alpha_t(x-1)^{1.7}+x} E_c \varepsilon & (x > 1) \end{cases} \tag{6}$$

where $\rho_t = f_t / E_c \varepsilon_{to}$ and $x = \varepsilon / \varepsilon_{to}$. $f_t$ is the axial tensile strength of the concrete, $\varepsilon_{to}$ is the strain corresponding to $f_t$, and $\alpha_t$ is the parameter of the descending stage.

Regarding the concrete confined in steel tubes, the constitutive model proposed by Han et al. (2007) was adopted, which is expressed as

$$y = \begin{cases} 2x - x^2 & (x \le 1) \\ \frac{x}{\beta_0(x-1)^\eta+x} & (x > 1) \end{cases} \tag{7}$$

where $x = \varepsilon / \varepsilon_o$, $y = \sigma / \sigma_o$, $\sigma_o = f_c'$, $\varepsilon_o = \varepsilon_c + 800\xi^{0.2} \times 10^{-6}$, $\eta = 1.6 + 1.5/x$, $\xi = f_y A_s / f_{ck} A_c$, $\varepsilon_c = (1300 + 12.5f_c') \times 10^{-6}$, and $\beta_0 = (f_c')^{0.1} / 1.2(1 + \xi)^{0.5}$.

In the above algorithm, $f_c'$ is the cylinder strength of the core concrete, and $\xi$ is the confinement coefficient of the CFST column. $A_s$ and $A_c$ are the cross-sectional areas of the steel tube and core concrete, respectively. $f_y$ is the yield strength of the steel tube, and $f_{ck}$ is the axial compressive strength of the core concrete.

According to the above constitutive models, the stress versus strain relationship of the concretes employed in this study is shown in Fig. 20. For the concrete damage variables and stiffness recovery coefficients, the values reported by Li and Han (2011) were used.

### 4.3 Verification of FE Model

#### 4.3.1 Verification of Failure Modes

Figure 21 shows the predicted failure mode of specimen F-1. There is generally good agreement between the failure mode predicted by the FE model and that observed in the test. Serious local buckling occurs on both the lower column ends and the upper column ends. According to the observed values of the plastic strain magnitude (PEMAG), the plastic strains of the lower column ends are higher than those of the upper column ends; the plastic strain ratios between the upper and lower column ends are approximately 0.88 for the left column and 0.74 for the right column, which is consistent with the experimental results. Figure 22 shows the damage process of the SRC beam in the FE analysis. The bending cracks were first observed at the mid-span of the beam during the application of vertical loads. Then, the specimen entered its lateral loading stage. The typical characteristic of this stage was the development of diagonal cracks. When the specimen reached its yield state, diagonal through cracks connecting the beam loading point and the supports were formed. Thereafter, the diagonal cracks were constantly developed with the increase in the lateral loads. When the specimen reached its peak state, the plastic strains were mainly concentrated at the bottom of the beam ends, and the concrete crushing in the test reflected this phenomenon. When the specimen reached its ultimate state, the maximum value of the plastic strain was approximately four times higher than that in the peak state, which is consistent with the enlargement of the concrete crushing regions.
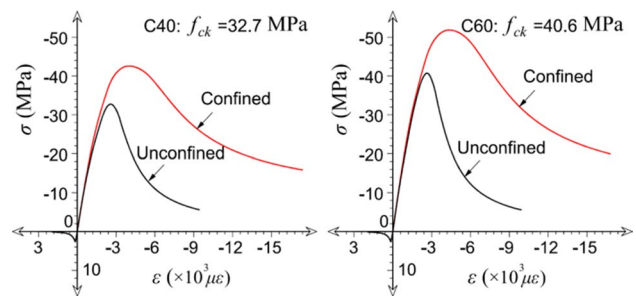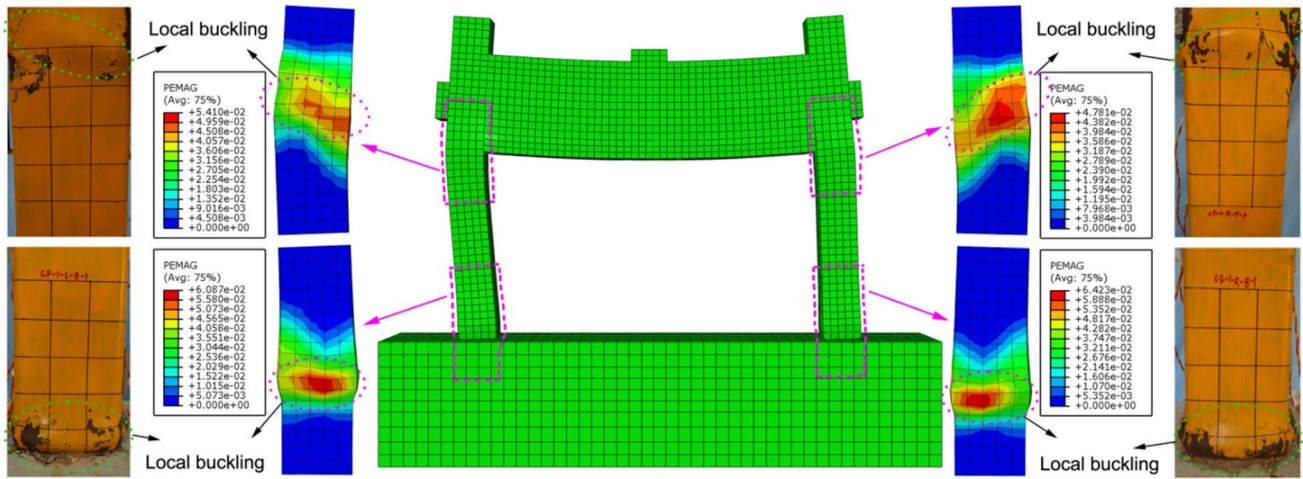


**Fig. 20** Stress–strain relationship for the concrete

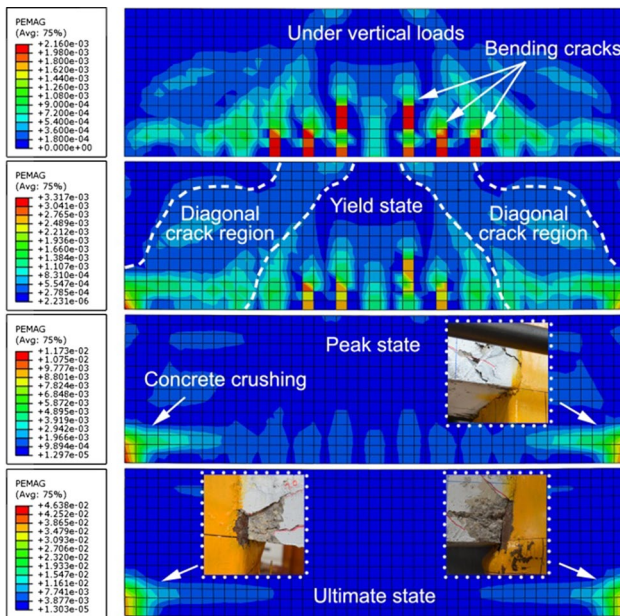**Fig. 21** Comparison of the observed and predicted failure modes



**Fig. 22** Predicted damage process of the beam

### 4.3.2 Verification of Load–Displacement Curves

The predicted and measured load–displacement relationships are compared in Fig. 23. There is good agreement between the predicted and experimental results. Regarding the shapes of the hysteretic curves and skeleton curves, the FE models provided a relatively reasonable prediction, although differences existed in the stiffness changes and residual bearing capacities, possibly because the constitutive models of the steel and concrete adopted in the FE model are certainly different from the stress–strain relationship of the actual materials. Additionally, the manufacturing deviations and test conditions impact the experimental results.

Regarding the ultimate bearing capacities of F-1, the values obtained from the FE results in the PD and ND are 453.7 and 450.9 kN, respectively, which are 4.3% and 3.1% lower, respectively, than those obtained from the experiments. Regarding the ultimate bearing capacities of F-2, the values obtained from the FE results in the PD and ND are 488.1 and 494.6 kN, respectively, which are 5.7% and 1.7% lower,
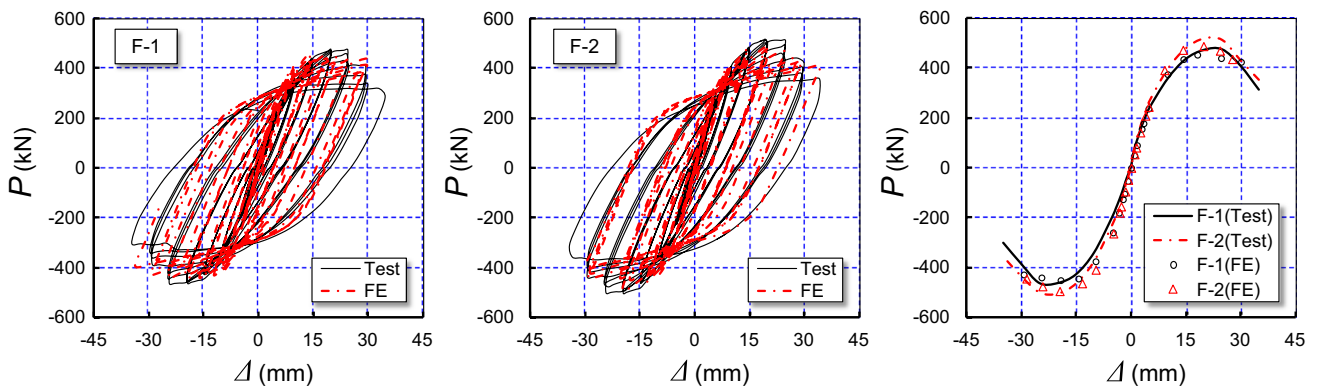


**Fig. 23** Comparison between the observed and predicted load–displacement relationships

respectively, than those obtained from the experiments. Overall, the differences between the predicted and measured bearing capacities are relatively small.

### 4.4 Parametric Study

To further investigate the seismic behavior of this kind of composite frame, parametric studies were performed. The concrete and steel grades were selected according to Chinese code GB 50010 (2010) and GB 50017 (2017), respectively. The reference frame specimen is described as follows.

The dimensions and details of the reference specimen are shown in Fig. 2. The grades of the beam concrete and column concrete are C40, and the corresponding axial compressive strength $f_{ck}$ is 26.8 MPa. The grades of the square steel tube and I-shaped steel are Q345, and the corresponding yield strength $f_y$ is 345 MPa. The grades of the longitudinal steel bars and stirrups are HRB400 and HPB300, respectively. The axial compression ratio of the column is 0.4 according to Eq. (1). The vertical load applied on the beam is 0.8 times its yield bearing capacity.

#### 4.4.1 Effect of Strength of Column Concrete

Regarding the concrete in the square steel tube, high-strength concrete can lead to an increase in the structural bearing capacity. Three types of concrete were selected for the core concrete to study their effects on the seismic behavior of the frames. The concrete grades are C40, C60, and C80, and the corresponding axial compressive strengths are 26.8, 38.5, and 50.2 MPa, respectively. The corresponding Young's moduli are $3.25 \times 10^4$, $3.6 \times 10^4$, and $3.8 \times 10^4$ MPa, respectively.

Figure 24 shows the skeleton curves of the composite frames with different column concrete strengths. The corresponding ultimate bearing capacity ($P_{max}$) and ductility ($\mu$) are presented in Fig. 25. As shown in Fig. 24, the column
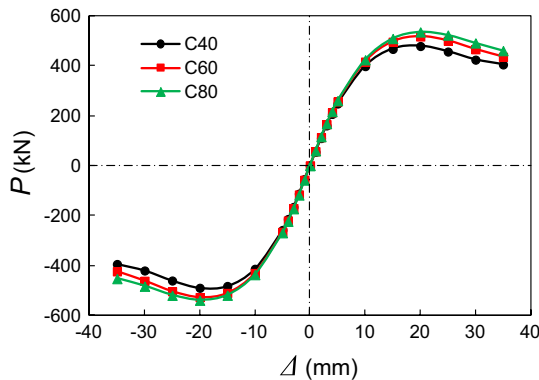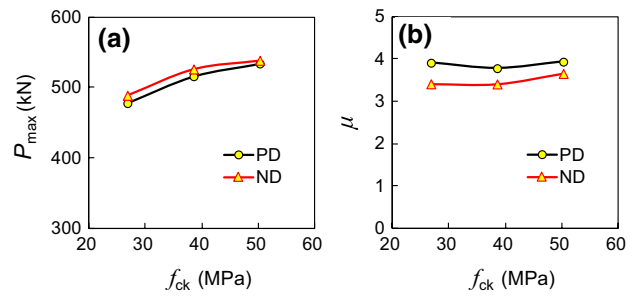
**Fig. 25** Effect of the strength of the column concrete on $P_{max}$ and $\mu$

concrete strength has no significant effect on the skeleton curves. Figure 25a indicates that the increase in the column concrete strength leads to a slight increase in the ultimate bearing capacity. When the concrete strength grade increases from C40 to C60 and C80, the average ultimate bearing capacity $P_{max}$ (mean value in the PD and ND) is found to increase by 7.8% and 10.9%, respectively. Additionally, Fig. 25b shows that the concrete strength has little influence on the ductility.

#### 4.4.2 Effect of Strength of Steel Tube

In practice, Q235, Q345, and Q460 steels are typically used for engineering design, and their yield strengths are 235, 345, and 460 MPa, respectively. The main purpose of using a high-strength steel for CFST columns is to improve the structural bearing capacity, owing to their high strength and good confining effect. These three kinds of steels were selected for investigation.

Figure 26 shows the effects of the yield strength of the steel tube on the $P - \Delta$ skeleton curves. The comparisons of the curves show that the yield strength has a remarkable effect on the $P - \Delta$ relationship. Figure 27 shows the effects of the yield strength on $P_{max}$ and $\mu$, indicating that the average $P_{max}$ increases by 21.4% and 39.9% as the steel
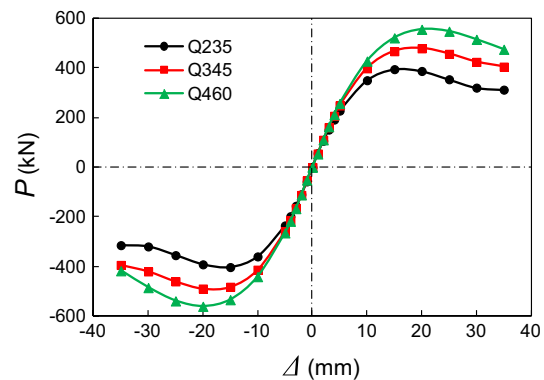
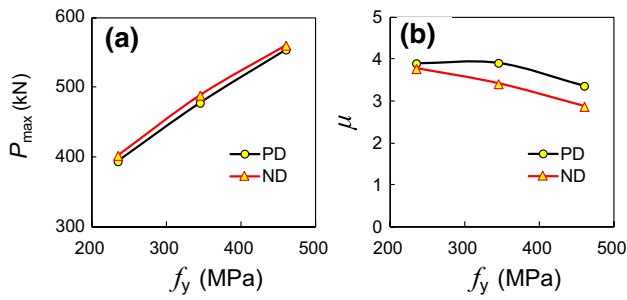**Fig. 24** Effect of the strength of the column concrete on the skeleton curves

**Fig. 26** Effect of the strength of the steel tube on the skeleton curves

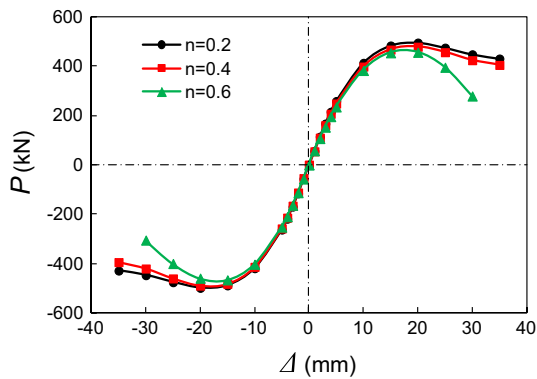**Fig. 27** Effect of the strength of the steel tube on $P_{max}$ and $\mu$



**Fig. 30** Effect of the beam load on the skeleton curves



**Fig. 28** Effect of the axial compression ratio on the skeleton curves



**Fig. 31** Effect of the beam load on $P_{max}$ and $\mu$

axial compression ratio has a great effect on the $P$-$\Delta$ relationship of the frames, especially for the descending branch of the skeleton curve. Moreover, increasing the axial compression ratio from 0.2 to 0.4 and 0.6 reduces the average $P_{max}$ of a composite frame by 2.6% and 7.2%, respectively. Even worse, when the axial compression ratio increases from 0.2 to 0.4 and 0.6, the average $\mu$ is found to decrease by 13.9% and 26.1%, respectively.

### 4.4.4 Effect of Beam Load

According to the seismic design code (JTG/T B02-01-2008 2008), the load bearing level of the protected components must be determined according to the earthquake level. For the frame used in this study, the SRC beam is a protected component, which must be designed on the basis of the earthquake level. For the convenience of this study, the vertical loads ($N_b$) applied on the beam were determined as $0.6N_{by}$, $0.8N_{by}$, and $1.0N_{by}$, where $N_{by}$ is the yield bearing capacity of the SRC beam. Figure 30 shows the skeleton curves of composite frames with different $N_b$ values, and the effects of $N_b$ on the ultimate bearing capacity ($P_{max}$) and ductility ($\mu$) are presented in Fig. 31. The skeleton curves of the frames with different $N_b$ values are almost the same; only a slight difference is observed at the descending branch of
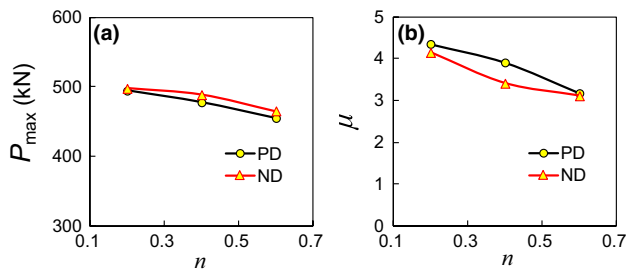


**Fig. 29** Effect of the axial compression ratio on $P_{max}$ and $\mu$

grade increases from Q235 to Q345 and Q460, respectively. In contrast, the average $\mu$ decreases by 4.6% and 18.7% as the steel grade increases from Q235 to Q345 and Q460, respectively.

### 4.4.3 Effect of Axial Compression Ratio

The axial compression ratio has a remarkable effect on the seismic behavior of a structure (Li et al. 2003). Axial compression ratios ranging from 0.2 to 0.6 for composite frames were studied. Figure 28 shows the skeleton curves of frames with different axial compression ratios, and Fig. 29 shows the effects of the axial compression ratio on $P_{max}$ and $\mu$. The
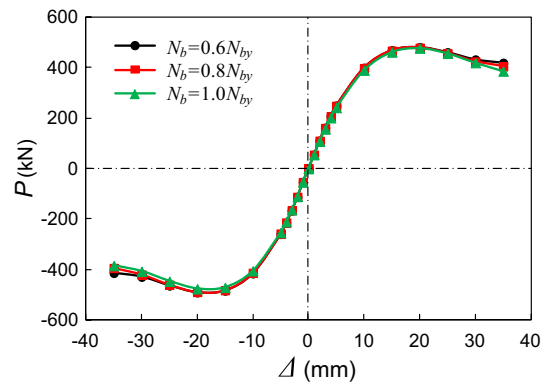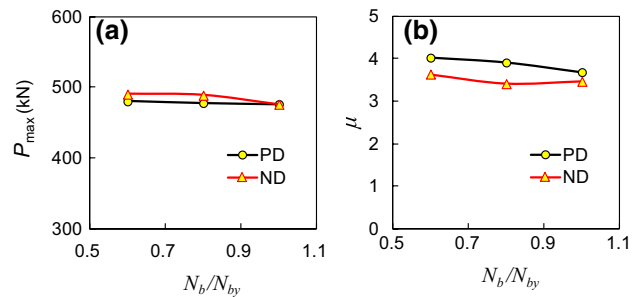
the skeleton curves. As shown in Fig. 31a, when the applied vertical load increases from $0.6N_{by}$ to $0.8N_{by}$ and $1.0N_{by}$, the average $P_{max}$ decreases by 0.4% and 1.8%, respectively. Hence, the effect of $N_b$ on $P_{max}$ is almost negligible. Additionally, increasing the vertical load ($N_b$) from $0.6N_{by}$ to $0.8N_{by}$ and $1.0N_{by}$ reduces the average $\mu$ of a composite frame by 4.4% and 6.7%, respectively. A possible reason for these changes is that increasing the vertical load ($N_b$) on the beam can increase the bending moments of the columns (in the vertical loading state), which means that the increase in $N_b$ can lead to an increase in the initial stress of the columns. Hence, the damages of the frame with a higher $N_b$ are more serious under earthquake excitation.

# 5 Conclusions

Two composite frames with the initial heavy load conditions were tested under cyclic loading, and some important seismic indices were discussed in detail. Additionally, a FE model for the tested composite frames was proposed for further investigations. According to the test results and numerical analysis, the following conclusions are drawn.

1. The experimental observations and failure modes for the two specimens were similar, and local buckling occurred at the lower and upper column ends, leading to the final failure of the specimens.
2. The hysteretic curves for the two specimens are comparatively plump and full, exhibiting a spindle shape, which indicates perfect seismic performance. However, the ultimate bearing capacity and initial stiffness of the specimen with high-strength concrete are relatively high.
3. The ductility factor of the tested specimens is in the range of 3.49 to 3.75. According to NZS 1170.5, this kind of composite frame can be regarded as a high-ductility structure. Moreover, both specimens showed a good energy dissipation capacity.
4. The numerical results of the tested composite frames achieved good agreement with the experimental observations. Regarding the effect of the typical parameters, it can be concluded that increasing the yield strength of the steel tube can effectively improve the bearing capacity of the composite frame and decreasing the axial compression ratio is an effective method for improving the ductility of the structure.
5. Although the composite frames tested in this study exhibited good seismic performance, the number of tested specimens was not high enough. Therefore, it is hard to make an overall evaluation for the seismic behaviors of this kind of composite frame. For in-depth research on this frame, more parameters should be investigated in future experiments, such as the steel

ratio, confinement factor, steel grade, cross section of the components, and loading level.

# References

ATC-24 (1992) Guidelines for cyclic seismic testing of components of steel structures. Applied Technology Council, Redwood City

Bazaez R, Dusicka P (2016) Cyclic behavior of reinforced concrete bridge bent retrofitted with buckling restrained braces. Eng Struct 119:34–48. https://doi.org/10.1016/j.engstruct.2016.04.010

Bhattacharya S, Hyodo M, Nikitas G et al (2018) Geotechnical and infrastructural damage due to the 2016 Kumamoto earthquake sequence. Soil Dyn Earthq Eng 104:390–394. https://doi.org/10.1016/j.soildyn.2017.11.009

Chen QJ, Cai J, Bradford MA et al (2014) Seismic behaviour of a through-beam connection between concrete-filled steel tubular columns and reinforced concrete beams. Eng Struct 80:24–39. https://doi.org/10.1016/j.engstruct.2014.08.036

Dong HH, Du XL, Han Q et al (2017) Performance of an innovative self-centering buckling restrained brace for mitigating seismic responses of bridge structures with double-column piers. Eng Struct 148:47–62. https://doi.org/10.1016/j.engstruct.2017.06.011

El-Bahey S, Bruneau M (2011) Buckling restrained braces as structural fuses for the seismic retrofit of reinforced concrete bridge bents. Eng Struct 33:1052–1061. https://doi.org/10.1016/j.engstruct.2010.12.027

Fujikura S, Bruneau M (2012) Dynamic analysis of multihazard-resistant bridge piers having concrete-filled steel tube under blast loading. J Bridge Eng 17:249–258. https://doi.org/10.1061/(ASCE)BE.1943-5592.0000270

Fulmer SJ, Nau JM, Kowalsky MJ et al (2016) Development of a ductile steel bridge substructure system. J Constr Steel Res 118:194–206. https://doi.org/10.1016/j.jcsr.2015.11.012

GB 50009–2012 (2012) Load code for the design of building structures. MOHURD, Beijing

GB 50010 (2010) Code for design of concrete structures. Ministry of Construction of the People's Republic of China, Beijing

GB 50017 (2017) Code for design of steel structures. Ministry of Construction of the People's Republic of China, Beijing

GB 50936–2014 (2014) Technical code for concrete filled steel tubular structures. MOHURD, China

GB, T 50081–2016 (2016) Standard for test method of mechanical properties on ordinary concrete. MOHURD, Beijing

GB, T228-2002 (2002) Metallic materials-tensile testing at ambient temperature. China Standards Press, Beijing

Han LH (2007) Concrete-filled steel tubular structures-Theory and practice (second version). China Science Press, Beijing

Han LH, Yao GH, Tao Z (2007) Performance of concrete-filled thin-walled steel tubes under pure torsion. Thin-Walled Struct 45:24–36. https://doi.org/10.1016/j.tws.2007.01.008

Han LH, Li W, Bjorhovde R (2014) Developments and advanced applications of concrete-filled steel tubular (CFST) structures: members. J Constr Steel Res 100:211–228. https://doi.org/10.1016/j.jcsr.2014.04.016

Ichikawa S, Matsuzaki H, Moustafa A et al (2016) Seismic-resistant bridge columns with ultrahigh-performance concrete segments.

J Bridge Eng 21:04016049. https://doi.org/10.1061/(ASCE)BE.1943-5592.0000898

JGJ, T 101–2015 (2015) Specification for seismic test of buildings. Architecture Industrial Press of China, Beijing

JGJ, T-281-2012 (2012) Technical specification for application of high strength concrete. MOHURD, Beijing

JTG, T B02–01-2008 (2008) Guidelines for seismic design of highway bridges. Ministry of Transport of the People's Republic of China, Beijing

Li W, Han LH (2011) Seismic performance of CFST column to steel beam joints with RC slab: analysis. J Constr Steel Res 67:127–139. https://doi.org/10.1016/j.jcsr.2010.07.002

Li JH, Su RKL, Chandler AM (2003) Assessment of low-rise building with transfer beam under seismic forces. Eng Struct 25:1537–1549. https://doi.org/10.1016/S0141-0296(03)00121-4

Li GC, Chen BW, Yang ZJ et al (2018) Experimental and numerical behaviour of eccentrically loaded high strength concrete filled high strength square steel tube stub columns. Thin-Walled Struct 127:483–499. https://doi.org/10.1016/j.tws.2018.02.024

Mohebbi A, Saiidi MS, Itani A (2015) Seismic evaluation of a precast PT/UHPC bridge column with pocket connection and precast footing. In: 2015 National accelerated bridge construction conference. Miami (USA)

Montejo L, Gonzalez-Roman LA, Kowalsky M (2012) Seismic performance evaluation of reinforced concrete-filled steel tube pile/column bridge bents. J Earthq Eng 16:401–424. https://doi.org/10.1080/13632469.2011.614678

Nie JG, Pan WH, Tao MX et al (2017) Experimental and numerical investigations of composite frames with innovative composite transfer beams. J Struct Eng 143:04017041. https://doi.org/10.1061/(ASCE)ST.1943-541X.0001776

NZS 1170.5 (2004) Structural design actions part 5: earthquake actions-New Zealand—commentary. Standards New Zealand, Wellington

Roeder CW, Stephens MT, Lehman DE (2018) Concrete filled steel tubes for bridge pier and foundation construction. Int J Steel Struct 18:39–49. https://doi.org/10.1007/s13296-018-0304-7

Sakino K, Nakahara H, Morino S et al (2004) Behavior of centrally loaded concrete-filled steel-tube short columns. J Struct Eng 130:180–188. https://doi.org/10.1061/(ASCE)0733-9445(2004)130:2(180)

Shahnewaz MD, Rteil A, Alam MS (2012) Seismic effects on deep beams in a reinforced concrete building. In: 3rd international structural specialty conference. Edmonton (Canada)

Stephens MT, Lehman DE, Roeder CW (2018) Seismic performance modeling of concrete-filled steel tube bridges: tools and case study. Eng Struct 165:88–105. https://doi.org/10.1016/j.engstruct.2018.03.019

Su RKL, Chandler AM, Lam NTK (2002) Seismic assessment of transfer plate high rise buildings. Struct Eng Mech 14:287–306. https://doi.org/10.12989/sem.2002.14.3.287

Tao MX, Fan JS, Nie JG (2013) Seismic behavior of steel reinforced concrete column–steel truss beam hybrid joints. Eng Struct 56:1557–1569. https://doi.org/10.1016/j.engstruct.2013.07.029

Wang W, Chen YY, Dong BP et al (2011) Experimental behavior of transfer story connections for high-rise SRC structures under seismic loading. Earthquake Eng. Struct. Dyn 40:961–975. https://doi.org/10.1002/eqe.1067

Wang Z, Wang JQ, Liu TX et al (2016) Modeling seismic performance of high-strength steel–ultra-high-performance concrete piers with modified Kent–Park model using fiber elements. Adv Mech Eng 8:1–14. https://doi.org/10.1177/1687814016633411

Wu Y, Cai J, Yang C et al (2011) Mechanical behaviours and engineering application of steel truss reinforced concrete transfer beam in tall buildings. Struct Des Tall Spec Build 20:735–746. https://doi.org/10.1002/tal.589

Zhao B, Taucer F, Rossetto T (2009) Field investigation on the performance of building structures during the 12 May 2008 Wenchuan earthquake in China. Eng Struct 31:1707–1723. https://doi.org/10.1016/j.engstruct.2009.02.039

Zhou L, Su YS (2018) Cyclic loading test on beam-to-column connections connecting SRRAC beams to RACFST columns. Int J Civ Eng 16(11):1533–1548. https://doi.org/10.1007/s40999-018-0288-x